

# Dual Constant Voltage Mode Control for Resonant Current Reduction in E-Bike's Low-Profile Wireless Charging System

Laskar Pamungkas<sup>1</sup>, Bo-Chih Shih<sup>2</sup>, Yu-Chen Chang<sup>2</sup>, and Huang-Jen Chiu<sup>2</sup>

<sup>1</sup> Country Representative Office (Indonesia KPPA), Yiqun (Enercentrik) Green Energy Tech. Co., Ltd., Taiwan

<sup>2</sup> Department of Electronic and Computer Engineering, National Taiwan University of Science and Technology, Taiwan

**Abstract--**This paper focuses on implementing a series-series (SS) resonant wireless power transfer (WPT) with a primary-side resonant current reduction while entering the constant voltage (CV) mode. The prototyping scale and the research methodology are conducted by referring to the electric bicycle (E-Bike) charging applications. Firstly, the basic principles of the WPT system are studied. Then the performance of the resonant tank parameters is analyzed under the switching frequency variation by the equivalent model of the WPT circuit. The conventional CC/CV control method is briefly explained, as well as its limitation. Afterward, the Dual Constant Voltage Mode (DCVM) is proposed to overcome that limitation, resulting in an efficiency improvement when the WPT system enters the light-load condition. Subsequently, the firmware is designed to achieve a practical CC/CV charging mode. Finally, a 200 Watt SS-WPT system with the DCVM optimization is built and experimentally tested in the 20 mm air-gap to verify the theoretical derivation. The power transfer efficiency can reach 90% at the full-load, and the light-load efficiency can be optimized, as the main contribution of this research.

**Index Terms**—Dual constant voltage mode, low-profile, resonant current, series-series, wireless power transfer.

## I. INTRODUCTION

Due to the increasingly intense issue of climate change, the awareness of environmental sustainability in various countries is increasing. Many international organizations have signed agreements to govern the trend of global warming. To reduce the air pollution and carbon emissions from transportation, many countries have further promoted the electrification of oil-fueled vehicles [1]. In the public transport sector, a railway system is electrified gradually, the mass rapid transit (MRT) and the electric light-rail train are developed, and the electric bus replaces the oil-fueled bus. Among people who use private vehicles, the trend of using electric vehicles (EV) is also increasing, such as electric scooters (E-Scooter) and bicycles (E-Bike) that are relatively affordable and have great flexibility [1, 2].

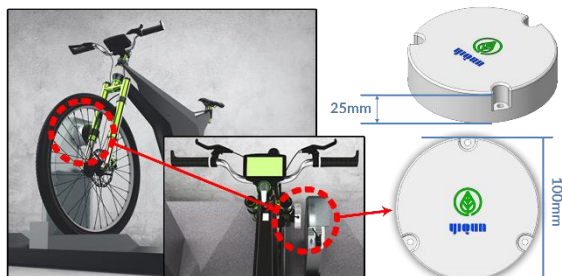


Fig. 1. Physical appearance of E-Bike's wireless charger.

Finally, an EV-based transportation system is formed. This trend made EVs become flourish, then their energy storage system and charging technology become essential parts of the global industries [2, 3]. The conventional EV charging system requires wire connections. For example, the MRT system needs to use overhead cables or third rails to provide electric power. EV cars also need to be charged through a plug-in charging connector, meanwhile, some E-Scooters use a battery swab system. However, the charging connectors will be exposed to moisture and rust due to outdoor applications, thereby significantly reducing the lifetime and harming the safety of the device. As another issue subjected, frequent charging also limits the mobility and ease of use of EVs [4]. Therefore, a wireless power transfer (WPT) system has received extensive attention from academia and business societies in these recent years. In addition to the needs in various special environments, such as human implantable devices, chemical industries, high-voltage infrastructures, underwater operations, and other power transfer applications, the popularity of WPT applications in daily life can also be clearly seen [5, 6].

This research focuses on WPT applications for an E-Bike's charging system, as illustrated in Fig. 1. Firstly, the basic principles of the WPT system are studied by applying the first harmonic approximation (FHA) model in the WPT circuit, as shown in Fig. 2. Afterward, the constant current and constant voltage (CC/CV) control is discussed, which is practically used in a battery charging scheme [7]. The limitation of the conventional control method is also examined, as well as the proposed solution, the Dual Constant Voltage Mode (DCVM), employed to overcome that limitation, resulting in an efficiency improvement when the WPT system enters the light-load condition. Instead of magnetic and material optimization of the couplers [8, 9], this paper will highlight the improvement of the WPT system by using a control methodology. The experimental results prove that the light-load efficiency can be optimized, as the main contribution of this research.

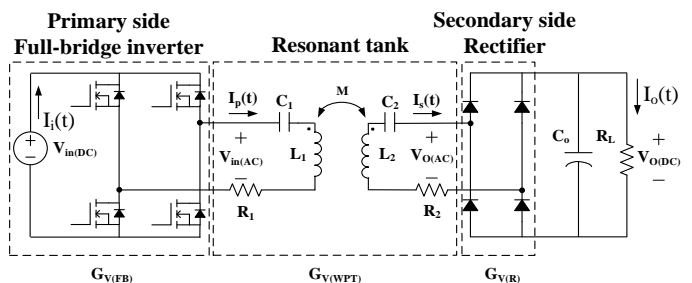


Fig. 2. Simplified WPT circuit with series-series resonant tank.

## II. SERIES-SERIES WPT SYSTEM MODELLING

In the WPT system, the transmitter (TX) coil transfers the power to the receiver (RX) coil through magnetic resonance. Generally, two different circuit models are used for the analysis. The first model is a coupled-inductance, which is identical to an induced voltage, and the second model is an ideal transformer, which is formed by the turn ratio, magnetizing, and leakage inductances. Logically, the variables of both methods can be equally converted.

As shown in Fig. 3(a), the coupled-inductance model has a pair of self-inductances,  $L_1$  and  $L_2$ , representing the primary and secondary sides, respectively. That pair of inductances will generate a mutual inductance,  $M$ , with the coupling strength indicated by the coupling coefficient,  $k$ . Hence, the induced voltages are generated on both sides, which are defined in  $V_{12}$  and  $V_{21}$ , depicted in Fig. 3(a).

By an ideal transformer representation, the transformer model is also commonly used as the analysis method in the WPT system, as drawn in Fig. 3(b). The parameters are symbolized by  $L_{lk1}$ ,  $L_{lk2}$ , and  $L_m$  for primary and secondary leakages, and the magnetizing inductances, respectively. Compared with the conventional transformers, the coupled coils of the WPT system have lower  $k$ . In other words, the values of  $L_{lk1}$  and  $L_{lk2}$  are higher, and  $L_m$  is smaller.

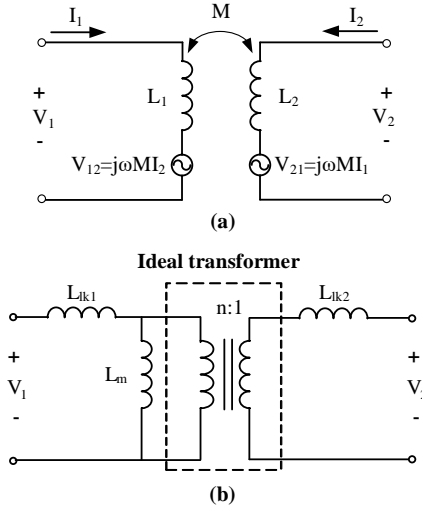


Fig. 3. WPT in the (a) coupled-inductance and (b) transformer models.

$$L_m = n \cdot M; \quad n = \frac{n_1}{n_2} = \sqrt{\frac{L_1}{L_2}} \quad (1)$$

$$L_{lk1} = L_1 - n \cdot M; \quad L_{lk2} = L_2 - \frac{M}{n} \quad (2)$$

The parameters in both circuit models can be equated according to the formulas in (1) and (2) above. Therefore, a pair of coils on the WPT system can be easily expressed in the mathematical model, and further combined with the other models from the front-side and back-side power converter circuits, as previously illustrated in Fig. 2.

### A. Voltage Gain Analysis of Series-Series WPT System

The voltage gain of the WPT system plays an important role in all operability analyses. In the basic study, it brings a completely procedural way of the component selections,

to fulfill the required WPT system specifications. In this research, the variable  $G_{V(Tot)}$  is used to state the voltage gain of the WPT system. Equivalently,  $G_{V(Tot)}$  consists of the gains of the primary-side's full-bridge inverter,  $G_{V(FB)}$ , the resonators,  $G_{V(WPT)}$ , and the secondary-side's rectifier,  $G_{V(R)}$ . As highlighted in this research, a key-equation of the primary-side's current analysis is derived from  $G_{V(Tot)}$ .

According to the power flow direction, the first part of  $G_{V(Tot)}$  is  $G_{V(FB)}$ . The full-bridge inverter converts the DC voltage source,  $V_{in(DC)}$ , into an AC square waveform in a positive and negative polarity,  $V_{in(AC)}$ , that ideally can be expressed by the Fourier series, by ignoring the high-order harmonic components. This assumption is taken when the switching frequency,  $F_{SW}$ , is not so far to the resonant frequency,  $F_R$ . Therefore, the first harmonic approximation (FHA) method is used to simplify it, as expressed in (3).

$$V_{in(AC)}(t) = \frac{4}{\pi} \cdot V_{in(DC)} \cdot \sin(2\pi ft) \quad (3)$$

$$V_{o(AC)}(t) = \frac{4}{\pi} \cdot V_{o(DC)} \cdot \sin(2\pi ft - \theta) \quad (4)$$

In the same assumption, the FHA method can also be used to simplify the part of  $G_{V(R)}$ . If the output voltage of the resonant tank,  $V_{o(AC)}$ , is the same form as  $V_{in(AC)}$ , and by considering the phase difference generated by the resonant tank,  $\theta$ , the function of  $V_{o(AC)}$  can be stated in (4) above.

$$i_s(t) = \sqrt{2} \cdot i_{s(rms)} \cdot \sin(2\pi ft - \theta) \quad (5)$$

$$i_o(t) \Leftrightarrow i_o = \frac{2\sqrt{2}}{\pi} \cdot i_{s(rms)} \quad (6)$$

The input current of the rectifier circuit,  $i_s$ , is expressed in (5) by using the FHA method. The output current of the rectifier is filtered by the output capacitor,  $i_o$ , in the DC form, which is considered as the average value of  $i_s$ , and the formula is expressed in (6). Subsequently, by using (4) and (6), the equivalent impedance of the rectifier can be described in the AC representation, as stated in (7) below.

$$R_{L(AC)} = \frac{V_{o(AC)}}{i_{s(rms)}} = \frac{8}{\pi^2} \cdot \frac{V_{o(DC)}}{i_o} = \frac{8}{\pi^2} \cdot R_L \quad (7)$$

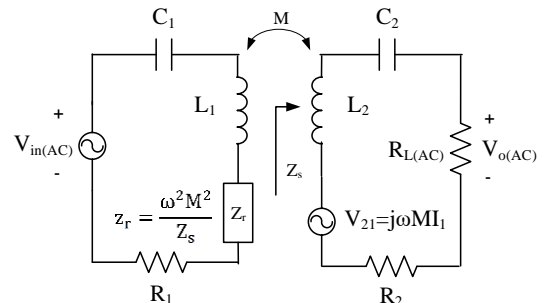


Fig. 4. FHA in coupled-inductance model of series-series WPT.

The expression of  $G_{V(WPT)}$  can be derived in both models of the series-series (SS) type WPT system. Fig. 4 above shows the FHA implementation in the coupled-inductance model. It introduces  $Z_s$ , as the equivalent impedance of the secondary-side, and  $Z_r$ , as the reflected impedance from the secondary-side to the primary-side. The WPT coil's

resistances are denoted by  $R_1$  and  $R_2$ , for the primary and the secondary sides, respectively. Finally, the final form of  $G_{V(WPT)}$  is stated in (8) for the coupled-inductance model.

$$\begin{aligned} G_{V(WPT)} &= \frac{j\omega M \cdot R_{L(AC)}}{(Z_p \cdot Z_s) + (\omega M)^2} \\ \left\{ \begin{array}{l} Z_p = j\omega L_1 + \frac{1}{j\omega C_1} + R_1 \\ Z_s = j\omega L_2 + \frac{1}{j\omega C_2} + R_2 + R_{L(AC)} \end{array} \right. \end{aligned} \quad (8)$$

The  $G_{V(WPT)}$  expression above informs the WPT system operability, so that the resonator values can be adjusted to meet the desired specifications. Only the value of  $R_{L(AC)}$  is independent of the resonant tank. As previously stated, the approximation of  $R_{L(AC)}$  is simplified by (7).

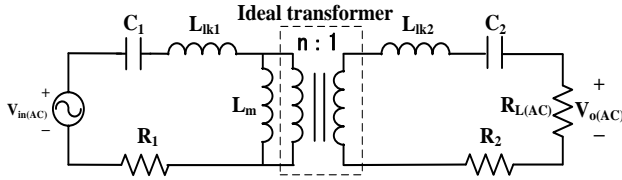


Fig. 5. FHA in transformer model of series-series WPT.

The same FHA method can also be used to generate the solution on a transformer model basis, as shown in Fig. 5. Hence, another  $G_{V(WPT)}$  expression is declared in (9).

$$\begin{aligned} G_{V(WPT)} &= \frac{n \cdot K \cdot R_{L(AC)}}{(Z_p + K) \cdot Z_s} \\ K &= \left( \frac{Z_s}{n^2} \right) \parallel M = \frac{Z_s \cdot M}{Z_s + n^2 M} \end{aligned} \quad (9)$$

#### B. Voltage Gain Plot using E-Bike's WPT Specifications

Based on the parameters of the WPT system utilized in this research, the characteristics of  $G_{V(WPT)}$  can be plotted in the function of  $F_{SW}$ , as shown in Fig. 6. The detailed specifications are listed in Table I. The values are tuned by considering the dimensional size in E-Bike applications.

The vertical redline in Fig. 6 indicates the zero-phase operating point,  $f_0$ , which can be calculated by:

$$f_0 = \frac{1}{2\pi\sqrt{L_1 \cdot C_1}} = \frac{1}{2\pi\sqrt{L_2 \cdot C_2}} \quad (10)$$

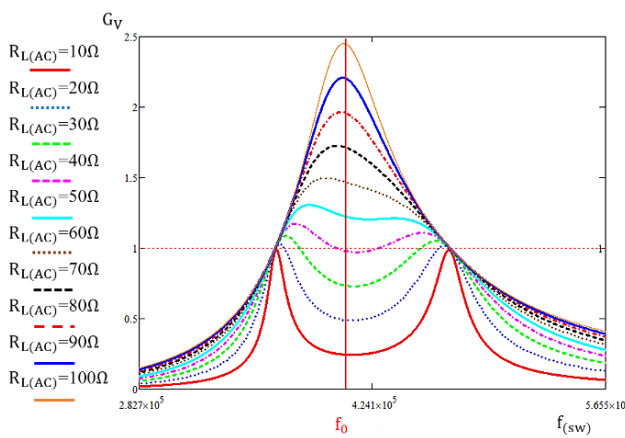


Fig. 6. Voltage gain curve plot of E-Bike's WPT system.

If the coupled coils are symmetrical, the value of  $F_R$  will be equal to  $f_0$ . When the circuit operates at this point, the advantage is that the phase difference between the input voltage and the input current is zero. Thus, the reactance is also zero at that time, and the primary-side inverter has a lower circulating current, resulting in a higher efficiency achievement. On the other hand, it also has a significant disadvantage in light-load conditions. Since the equivalent input impedance is lower, the input current will increase, then the efficiency will be degraded. At the same time,  $G_{V(WPT)}$  changes greatly, so the value of  $V_{o(AC)}$  will be hard to maintain, and the post-regulator stage may be required.

#### III. DUAL CONSTANT VOLTAGE MODE CONTROL FOR RESONANT CURRENT REDUCTION IN WPT SYSTEM

When the post-regulator stage is employed in the WPT system, the value of  $V_{o(AC)}$  is allowed to change in a certain range. Therefore, when the system operates in light-load conditions, the value of  $F_{SW}$  can be tuned to change the WPT input impedance,  $Z_{in}$ . According to (11),  $Z_{in}$  can be increased by increasing  $F_{SW}$ . Hence, the primary current,  $i_p$ , can be reduced to improve power efficiency,  $\eta$ . This is the main idea of the proposed dual constant voltage mode (DCVM) control. In the conventional method, the value of  $F_{SW}$  is always fixed in every load condition, so the primary-side inverter will continue to provide a large  $i_p$  due to the lower value of  $Z_{in}$ . As a result, a huge circulating current keeps flowing in the system and causes big power losses.

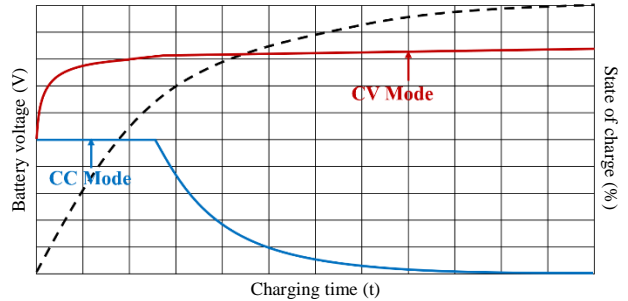


Fig. 7. Typical battery charging curve in CC and CV modes.

The CC/CV battery charging curves are illustrated in Fig. 7 above. When the system enters the CV mode, the load tends to be reduced gradually, and the charging time is longer in this situation. If  $i_p$  is reduced in this mode,  $\eta$  will be improved, and the power can be effectively saved.

TABLE I  
SPECIFICATIONS OF E-BIKE'S WIRELESS CHARGING SYSTEM

Parameter	Value
Input voltage - $V_{in(DC)}$	50 VDC
Output voltage - $V_{o(DC)}$	24 VDC
Output power - $P_o$	200 W
Switching frequency - $F_{sw}$	210 ~ 250 kHz
Self-inductance - $L_1$ & $L_2$	19.00 ~ 21.00 $\mu$ H
Mutual-inductance - $M$	8.00 ~ 8.25 $\mu$ H
Series capacitor - $C_1$ & $C_2$	40 nF
Coil dimension	90 mm × 90 mm
Air gap distance	20 mm

The expression of  $i_p$  in the SS-WPT system is shown in (12). In order to minimize  $i_p$ , the value of  $F_{SW}$  is increased. As mentioned earlier, this case will be happening in the lighter load while the WPT system enters the CV mode. At the same time,  $G_{V(WPT)}$  will also change when the load changes. Hence, we have to ignore the change of  $G_{V(WPT)}$  first and fix the value of  $G_{V(WPT)}$  by assuming the full-load condition. Another complicated way can be done by running the iteration between  $F_{SW}$ ,  $R_L$ , and  $G_{V(WPT)}$  changes, as the functions in (12). However, a simple fixed- $G_{V(WPT)}$  method is chosen in this research. Two different  $F_{SW}$  are analyzed in Mathcad software to see the main idea of this research. The  $i_p$  curve in 228 kHz and 242 kHz is plotted throughout the load conditions, as shown in Fig. 8 below.

$$Z_m = Z_p + Z_r = \left( j\omega L_1 + \frac{1}{j\omega C_1} + R_1 \right) + \left( \frac{\omega^2 \cdot M^2}{Z_s} \right) \quad (11)$$

$$i_p = \frac{\frac{2\sqrt{2}}{\pi} \cdot V_{in(DC)}}{Z_p + \frac{\omega^2 \cdot M^2}{Z_s + \left( \frac{(V_{in(AC)} \cdot G_{V(WPT)})^2}{P_{WPT}} \right)}} \quad (12)$$

It can be seen from Fig. 8 that when the output power of the WPT stage,  $P_{WPT}$ , is less than 120W, the value of  $i_p$  in  $F_{SW} = 242$  kHz is less than the value of  $i_p$  in  $F_{SW} = 228$  kHz. This phenomenon shows that if the value of  $F_{SW}$  is fixed at 228 kHz when the load changes from a heavy-load to a light-load, the WPT stage will maintain  $G_{V(WPT)}$ , and cause a higher value of  $i_p$ . If  $F_{SW}$  is tuned to 242 kHz, the WPT stage will have lower  $G_{V(WPT)}$ , and the value of  $i_p$  can be effectively reduced to improve  $\eta$  of the WPT system.

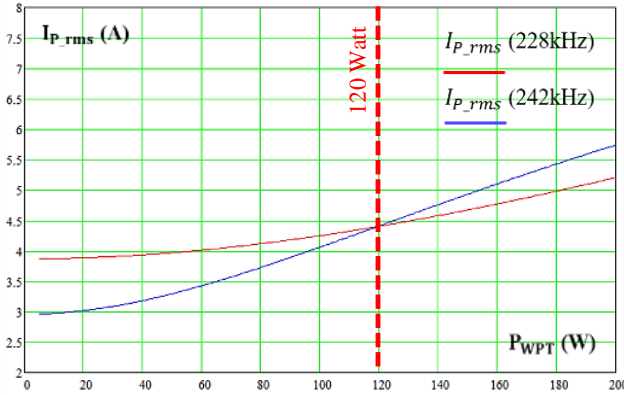


Fig. 8. Primary current versus load plot in 228 kHz and 242 kHz.

By using the same plotting method, two other  $F_{SW}$  are used to generate  $i_p$  versus  $P_{WPT}$  curves. One higher value (253 kHz) and one lower value (235 kHz) of  $F_{SW}$  are selected for the other plots, as shown in Fig. 9 and Fig. 10, respectively. The key parameters of this comparison study are recorded, especially the value of  $P_{WPT}$  when two  $i_p$  curves intersect each other, as presented in Table II.

It can be concluded from Table II that if the value of  $F_{SW}$  is lower, the load at the  $i_p$  curves intersectional point will be higher. When it is applied to the battery charging

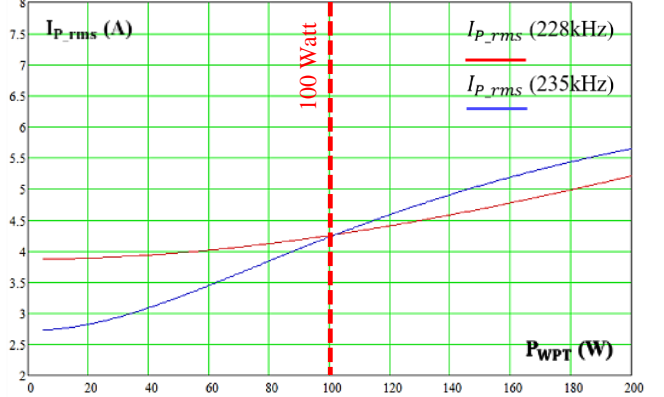


Fig. 9. Primary current versus load plot in 228 kHz and 253 kHz.

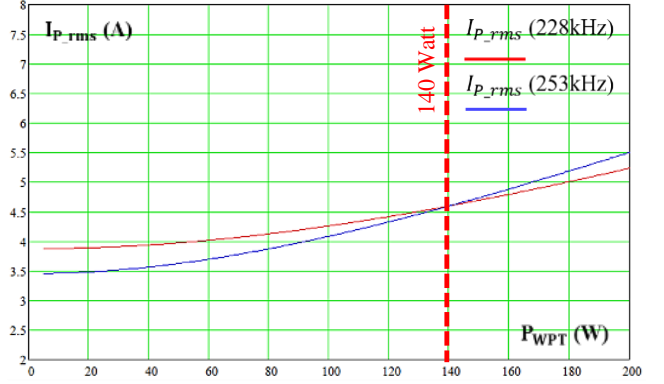


Fig. 10. Primary current versus load plot in 228 kHz and 235 kHz.

applications, the value of  $F_{SW}$  can be switched when the CV charging power reach  $P_{WPT}$  at  $i_p$  curves intersectional point. Hence, the value of the  $i_p$  can be reduced and a higher  $\eta$  can be obtained. This situation will result in two CV modes (each CV mode has different  $F_{SW}$ ) in the WPT system. Hence, this proposed method is called “Dual Constant Voltage Mode” or DCVM, as mentioned earlier.

By investigating the data from Table II, a  $F_{SW}$  value of 242 kHz is selected as the light-load CV mode, since it can reach  $i_p$  curves intersectional point faster than the 254 kHz  $F_{SW}$ , while performing a lower  $i_p$  compared to the 235 kHz.

TABLE II  
SUMMARY OF PRIMARY CURRENT CURVE VERSUS LOAD VARIATIONS  
COMPARED WITH THREE DIFFERENT SWITCHING FREQUENCIES

$F_{SW}$	$P_{WPT}$ at $i_p$ curves intersectional	$i_p$ value at %load		
		10%	20%	30%
235 kHz	140 Watt	3.5 A	3.6 A	3.7 A
242 kHz	120 Watt	3.0 A	3.2 A	3.4 A
254 kHz	100 Watt	2.8 A	3.1 A	3.3 A

#### IV. IMPLEMENTATION OF FIRMWARE CONTROLLER

The overall system control firmware in this paper is shown in Fig. 11. The primary-side and the post-regulator need each a set of control modules. The main task of the primary-side controller is to detect  $i_p$  and switch  $F_{SW}$  of the WPT system to perform the DCVM control. Afterward, the main task of the post-regulator controller is achieving a conventional CC/CV charging modes function according to the battery condition, as the load of the WPT system.

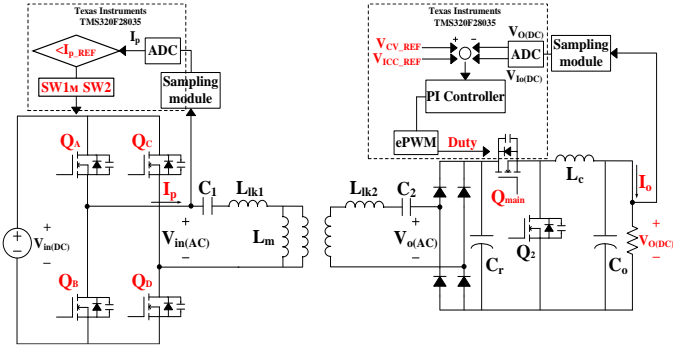


Fig. 11. Firmware diagram of WPT system with DCVM control.

The charging mode is divided into four modes, the first mode is trickle mode (TM), the second mode is CC mode, the third mode is CV mode I (CV-I) and the fourth mode is CV mode II (CV-II). The system control of TM, CC, and CV-I modes are majorly performed by the post-regulator stage. Otherwise, the primary-side controller will execute the system control of CV-II, with the DCVM method.

**1. From TM to CV-I:** In the system initialization mode, the post-regulator stage will be started with TM, and then the sensing circuit will scale-down  $V_{o(DC)}$  proportionally as a feedback voltage (0V ~ 3.3V), then the analog-to-digital converter (ADC) module in the TMS320F28035 control chip will converts it into a digital value for  $V_{o(DC)}$  reading. If the battery voltage,  $V_{Bat}$ , is less than  $V_{CV\text{-}Ref}$  (the voltage reference point for switching from CC to CV-I), then the WPT system will enter the CC mode control. However, if  $V_{Bat}$  is higher than  $V_{CV\text{-}Ref}$ , or has been charged to this point through the CC mode, the WPT system will enter the CV-I control. In this CC/CV-I mode, the switching devices are controlled by simple proportional-integral (PI) controller. If the sensing value is less than the reference, the controller increases the duty cycle of the switching devices in the synchronous buck converter, as illustrated in Fig. 11. Otherwise, if the sensing value is higher than the reference, the controller decreases the duty cycle. Finally, this control stage is performed using pulse width modulator (ePWM) module of the TMS320F28035 control chip from TI.

**2. From CV-I to CV-II:** When the system enters CV-I, the load of the WPT system is gradually decreased. At this time, the primary-side controller continues to detect  $i_p$  through the sensing circuit and calculate its RMS value. If the RMS value of  $i_p$  is less than the reference point,  $i_{p\text{-}Ref}$ , then  $F_{SW}$  will change from 228 kHz to 242 kHz, and slowly increase battery capacity to 100% state-of-charge (SoC).

## V. EXPERIMENTAL RESULT AND DISCUSSION

The waveforms measured in this paper are shown in Fig. 12 to Fig. 16. Among them, Fig. 12 and Fig. 13 are the measured waveforms at the full-load condition, 200 Watt. Fig. 14 and Fig. 15 are the measured waveforms at the light-load condition, 60 Watt, equal to the 30% load. From those experimental waveforms, it can be observed that the WPT system designed in this paper can achieve a steady  $V_{o(DC)}$  under the load variation, during the CV mode. It can be seen from Fig. 13 and Fig. 15 that the switching devices on the primary-side inverter can achieve the zero voltage

switching (ZVS) characteristics to reduce the switching losses. Fig. 16 shows the waveforms with 60 Watt load without DCVM control, and the value of  $i_p$  is 4.40 A. As a comparison, Fig. 14 shows the waveforms with DCVM control at 60 Watt load, and the value of  $i_p$  is 3.57 A. It can be summarized that the proposed control method in this research can effectively reduce  $i_p$  at light-load conditions.

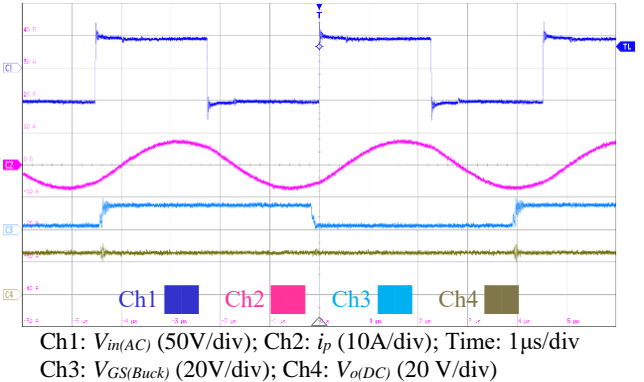


Fig. 12. Key-waveforms in 200 Watt as the full-load condition.

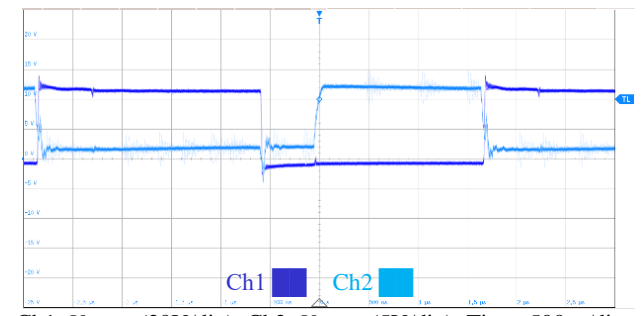


Fig. 13. ZVS characteristics in 200 Watt as the full-load condition.

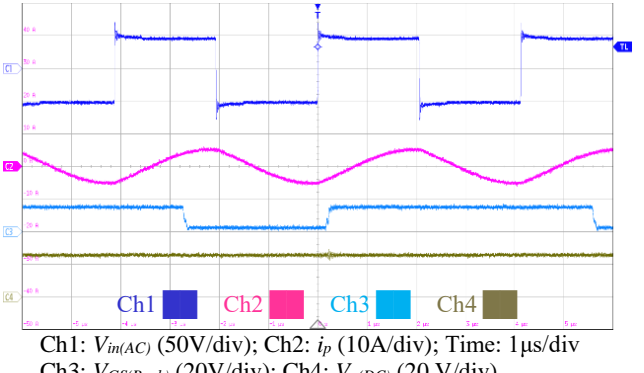


Fig. 14. Key-waveforms in 60 Watt as the 30% load condition.

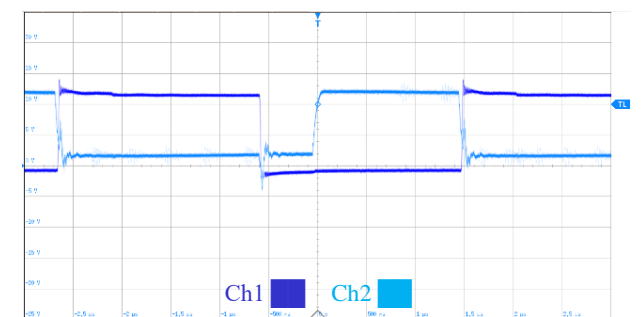


Fig. 15. ZVS characteristics in 60 Watt as the 30% load condition.

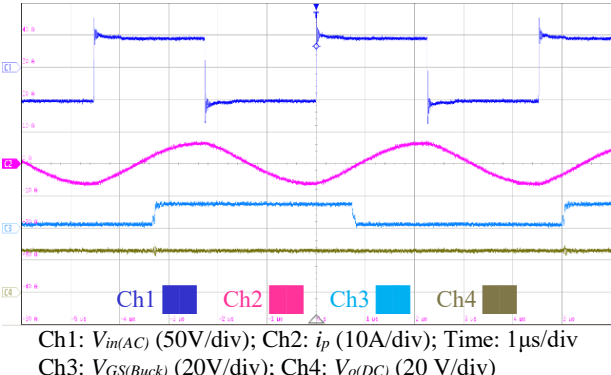


Fig. 16. Key-waveforms in 60 Watt but without DCVM control.

By measuring  $\eta$  of the WPT system under the load variation, the curve of  $\eta$  can be plotted in a graphical form. The measurement is conducted from 10% to 100% load conditions with the 10% step. The power-meter is used to guarantee the accuracy of the power measurement. The testing result of  $\eta$  curve with the proposed DCVM method is marked in the blue curve, as shown in Fig. 17 below. Meanwhile, the orange curve indicates the testing result of  $\eta$  curve without the proposed DCVM method. Finally, the  $\eta$  improvement can be clearly seen from Fig. 17. The improvement is 1.0% at 40% load, 2.8% at 30% load, 4.6% at 20% load and 8.4%  $\eta$  improvement at 10% load.

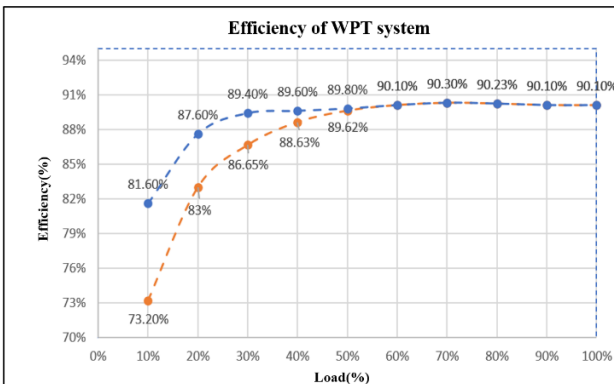


Fig. 17. Efficiency curves of WPT system in E-Bike applications (blue) with and (yellow) without proposed DCVM control.

## VI. CONCLUSIONS

The WPT system in this research is implemented in the E-Bike charging application. With the increasing number of the E-Bike market, the WPT system offers a reliable charging solution. By including the enclosure design consideration, the WPT system also can be used in outdoor charging applications. This research introduces the basic principles of common WPT concepts, employs the FHA method for simple modeling, and shows the limitation of the conventional CC/CV modes in the WPT system. By adopting the circular coil and SS resonant tank topology to develop the circuit, the equivalent model of the SS-WPT circuit is used to investigate the performance of the resonant tank while operating at the different  $F_{SW}$ .

The common control method is briefly explained, and the post-regulator stage is utilized to perform the CC/CV control. According to the  $F_{SW}$  selection and the control

circuit characteristics, the value of  $i_p$  is investigated by the mathematical analysis and curve-plotting method. Hence, the proposed DCVM control method is highlighted to overcome the problem of a higher  $i_p$  value. The study also includes the battery charging characteristics and the firmware control implementation for charging operability.

Finally, a 200 Watt SS-WPT system with the proposed DCVM control is experimentally tested at the prototyping stage. The air-gap distance between the two coupled coils of the WPT is 20 mm. The WPT can charge the battery in the CV/CC mode. The efficiency can reach 90% at full-load, and it can be optimized at a light-load by performing CV-II mode, as proven in some captured key-waveforms.

## ACKNOWLEDGMENT

The authors would like to acknowledge the financial support from the National Science and Technology Council – Taiwan through the grant number NSTC 111-2622-8-011-014 -SB.

## REFERENCES

- [1] H. Ribberink and E. Entchev, "Electric vehicles - a 'one-size fits-all' solution for emission reduction from transportation" 2013 World Electric Vehicle Symposium and Exhibition (EVS27), Barcelona, 2013, pp. 1-7.
- [2] B. Frieske, M. Kloetze and F. Mauser, "Trends in vehicle concept and key technology development for hybrid and battery electric vehicles," 2013 World Electric Vehicle Symposium & Exhibit. (EVS27), Barcelona, 2013, pp. 1-12.
- [3] J. K. Nama, M. Srivastava and A. K. Verma, "Modified inductive power transfer topology for electrical vehicle battery charging using auxiliary network to achieve zero-voltage switching for full load variations," *IET Power Electronics*, vol. 12, no. 10, 2019, pp. 2513–2522.
- [4] J. K. Nama and A. K. Verma, "An Efficient Wireless Charger for Electric Vehicle Battery Charging," 2020 IEEE 9th Power India International Conference (PIICON), Sonepat, 2020, pp. 1-4.
- [5] M. Granovskii, I. Dincer and M. A. Rosen, "Economic and environmental comparison of conventional, hybrid, electric and hydrogen fuel cell vehicles," *Journal of Power Sources*, vol. 159, no. 2, 2006, pp. 1186–1193.
- [6] Y. Zhou, M. Wang, H. Hao, L. Johnson and H. Wang, "Plug-in electric vehicle market penetration and incentives: a global review," *Mitigation and Adaptation Strategies for Global Change*, vol. 20, no. 5, 2015, pp. 777–795.
- [7] C. Zheng et al., "High-Efficiency Contactless Power Transfer System for Electric Vehicle Battery Charging Application," *IEEE Journal of Emerg. and Selected Topics in Power Electronics*, vol. 3, no. 1, March 2015, pp. 65-74.
- [8] Y. Zhou and A. M. Sun, "Simplified ferrite core loss separation model for switched mode power converter," *IET Power Electronics*, vol. 9, no. 3, 2016, pp. 529–535.
- [9] H. Zhao et al., "An Improved Core Loss Model of Ferromagnetic Materials Considering High-Frequency and Nonsinusoidal Supply," in *IEEE Transactions on Industry Applications*, vol. 57, no. 4, July-Aug. 2021, pp. 4336-4346.